RSC Advances

PAPER

View Article Online
View Journal | View Issue

Cite this: *RSC Adv.*, 2020, **10**, 27377

Facile photocatalytic reduction of carcinogenic Cr(VI) on Fe-doped copper sulfide nanostructures†

Noor ul Ain, Zia ur Rehman,* Ujala Nayab, Jamal Abdul Nasir and Asma Aamir

Received 1st June 2020
Accepted 3rd July 2020

DOI: 10.1039/d0ra04852f

rsc.li/rsc-advances

In this study, Fe-doped copper sulfide nanoparticles (NPs) were investigated for the solar-assisted reduction of Cr^{VI} ions in raw water. The Fe-doped NPs were synthesized by decomposing copper(II) *N*,*N*-diphenylmethylpiperazinecarbamodithioate *via* a facile single-step, one-pot solvothermal method in the presence of iron salt. The Cr^{VI} photoreduction data were fit to a pseudo-first-order kinetic model and a Langmuir model. The CuS/Cu_2S NP reduction ability for Cr^{VI} increases with an increase in dopant percentage. The best catalyst (9% Fe-doped) was able to reduce Cr^{VI} (10^{-4} M $K_2Cr_2O_7$) to Cr^{III} in raw water using an initial amount of 10 mg in 6 min with a reduction efficiency of up to 100%. The photocatalytic activity was examined while varying five different parameters: sunlight, diffused light, change in pH, and changes in the concentration of the catalyst and the temperature. This new approach presents an active, simple, and cost-effective means for wastewater treatment.

1. Introduction

Currently, an innovative technology built on the photocatalysis of an aqueous suspension of nanoparticles has received substantial consideration. The photocatalysis has been used for the quick and effective removal of environmental contaminants.[1] The solar light with an energy more than the semiconductor's band gap sequentially generates electron–hole pairs in the conduction and the valence bands (VB). These charge carriers (electron–hole pairs) are responsible for oxidizing or reducing pollutants in solution, provided that they have appropriate redox potentials. An innovating application of solar light-driven photocatalytic process involves the elimination of toxic metals, like chromium, lead and mercury, from industrial surplus water. The metals are reduced on the catalyst's surface and can be successfully removed from the resulting slurries by chemical or mechanical means[2] or they can be converted to less harmful materials.[3–6]

Chromium, an important inorganic element, exists commonly as the Cr^{VI} and Cr^{III} forms in both naturally and anthropogenically modified waters. The former is injurious to human health and is classified as both mutagenic and carcinogenic. It has been declared a primary pollutant by the EPA (US Environmental Protection Agency) owing to its high solubility, high toxicity and easy accumulation.[7–9] The World Health Organization (WHO) has recommended 0.1 ppm as the permitted limit of Cr^{VI} in inland water and 0.05 ppm in drinking water. Cr^{VI} exists in water as different oxyanions as a function of pH, *i.e.*, chromate (CrO_4^{2-}), hydrogen chromate ($HCrO_4^{1-}$) and dichromate ($Cr_2O_7^{2-}$). Hence, the conversion of lethal Cr^{VI} into ecofriendly Cr^{III} can be an important remediation approach to evade the venomous effects of Cr^{VI} on human health. Cr^{III} is less poisonous and considered as an indispensable micronutrient for human health.[10]

Several methods have been described for Cr^{VI} reduction, involving ion exchange, adsorption, membrane filtration, chemical precipitation, solvent extraction and electrocoagulation. Most of these techniques, however, are accompanied by problems, such as sludge disposal, formation of secondary pollutants, high capital cost, and high power depletion. These are the reasons why these techniques are not widely used. In contrast, photocatalysis is gaining attention as it is an economically inexpensive, viable and eco-friendly technique. Various reductants are being used for hexavalent chromium reduction, such as H_2S, HCOOH, Fe(II)-bearing minerals and Fe(0).[11] HCOOH is the most favorable for the reduction of Cr^{VI} among these reductants owing to its production of relatively environment friendly by-products, mild reaction conditions, and ready availability.

Copper sulfide (Cu_xS) is an eminent p-type semiconductor that has diverse uses in the fields of electronics, chemical sensing, photocatalysis, and batteries. In the last decade, it has attained great consideration in the area of catalysis because of its intriguing properties, high catalytic efficiency, nontoxicity, low price and tunable band gap (1.2–2.5 eV) in the visible region depending upon the stoichiometric composition from $x = 1$ to 2.[12] These features make CuS possibly an ideal light-harvesting and charge-transport material in photocatalysis. However, the solar-driven electron transfer process is restricted by recombination that

Department of Chemistry, Quaid-i-Azam University, Islamabad-45320, Pakistan. E-mail: zrehman@qau.edu.pk; hafizqau@yahoo.com; Fax: +92-51-90642241; Tel: +92-51-90642245

† Electronic supplementary information (ESI) available. See DOI: 10.1039/d0ra04852f

quenches the photocatalytic efficiency. The most efficient way to improve the photocatalytic activity is to dope the material with suitable transition metals. In our work, Fe^{II} is used as the dopant because it has a sufficiently positive reduction potential to draw electrons from CuS and thus prevent recombination of the charges. Moreover, the quantum-confinement effect in the semiconductor shifts the conduction band (CB) to a more negative value, thereby facilitating the shift of electrons from the catalyst's surface to the adsorbed reactant molecules.[13]

2. Experimental

2.1 Materials

In the following experiments, $CuCl_2 \cdot 2H_2O$, $K_2Cr_2O_7$, $Pb(NO_3)_2$ and $FeCl_2 \cdot 2H_2O$ were purchased from Merck, NaOH from Fluka, and *N*,*N* diphenylmethylpiperazine, DMF, CS_2, LR grade formic acid and ethylenediamine were purchased from Sigma-Aldrich. The analytical quality chemicals and solvents were used as received.

2.2 Preparation of single source precursor

The dithiocarbamate ligand and the copper complex were prepared according to our previously reported procedures.[14] An aqueous solution of $CuCl_2 \cdot 2H_2O$ was prepared by dissolving 0.160 g (0.938 mmol) of the salt in deionized water (30 mL). To this solution, an aqueous solution (30 mL) containing 0.5 g (1.83 mmol) of sodium 4-benzhydrylpiperazine-1-carbodithioate (Scheme 1) was added. After 3 h of vigorous stirring, the brown precipitates formed were filtered, washed several times with cold water, and dried. Yield: 0.373 g, 73.3%. Mp: 262–264 °C. FTIR (cm^{-1}): 1489, νC–N; 968, νC–S; 360, νCu–S.

2.3 Synthesis of CuS/Cu_2S and Fe-doped CuS/Cu_2S nanostructures

The CuS/Cu_2S and $Cu_{1-x}Fe_xS$ (x = 1, 3, 5, 7 and 9%) nanostructures were readily synthesized by a thermal decomposition procedure using a single source precursor (Scheme 1). About 1 g of the dried complex, together with x grams of $FeCl_2 \cdot 2H_2O$ (x = 0, 0.01, 0.03, 0.05, 0.07, 0.09 g), were added into a two-necked flask fitted with a condenser on one neck and a bent tube on the second that is connected to a test tube containing aqueous lead nitrate solution. About 15 mL of ethylenediamine was added and heated up to 180 °C for about 3 h. As the reaction progressed, the released H_2S gas that was formed led to the production of PbS in the test tube containing the aq. $Pb(NO_3)_2$

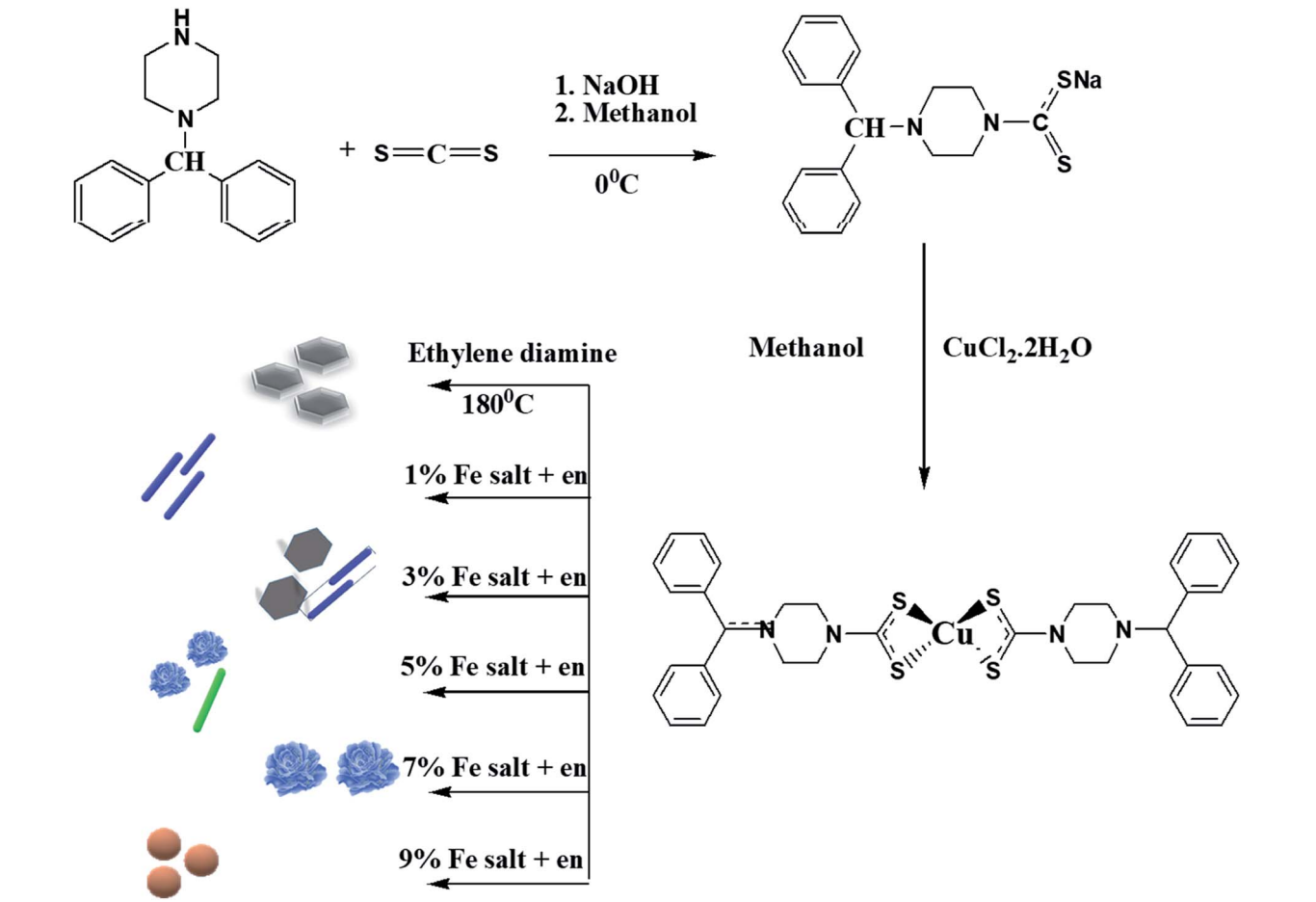

Scheme 1 Synthesis of single source precursor, CuS/Cu_2S and Fe-doped CuS/Cu_2S.

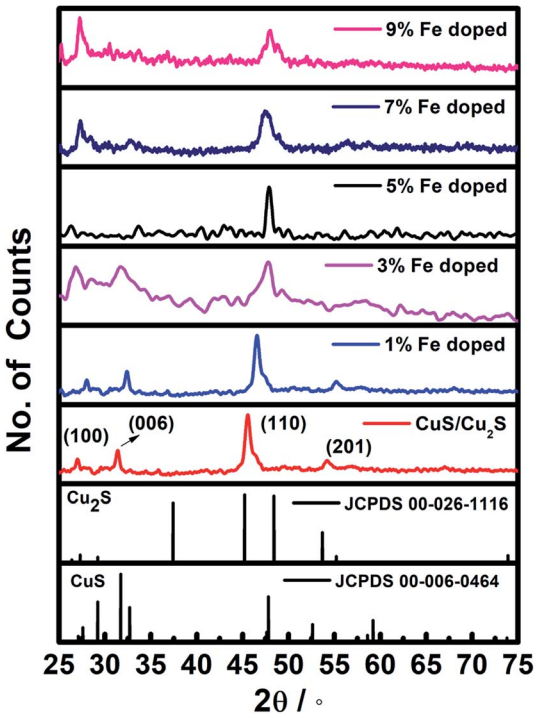

Fig. 1 XRD pattern of CuS/Cu_2S and (1, 3, 5, 7, 9%) Fe doped CuS/Cu_2S NPs.

solution. Eventually, black Fe-doped CuS/Cu_2S nanoparticles were obtained. These nanoparticles were filtered off, washed thoroughly with methanol several times and dried at room temperature. The proposed mechanism for the synthesis of nanoparticles is shown in Scheme S1 in the ESI.†

2.4 Characterization

Scanning electron microscopy was carried out using a Schottky Field Emission JEOL JSM-7600F instrument operational at an accelerating voltage of 0.1 to 30 kV. An Energy Dispersive X-ray Analyzer (EDX) was used to confirm the purity of the material. Powder X-ray diffraction analysis was performed on a PAN-analytical X'Pert^3 PRO Powder instrument fitted with Cu Kα radiation ($\lambda = 1.54178$ Å). UV-vis analysis of the Fe-doped CuS/Cu_2S nanoparticles was done on a Shimadzu double-beam spectrophotometer model 1800. A Nicolet 6700 Infrared Spectrophotometer (Thermo Scientific, USA) was used to measure the FTIR spectra of the complexes and the ligand. X-ray Photoelectron Spectroscopy (XPS) was done to confirm the oxidation states using a Thermo Scientific K-alpha Photoelectron Spectrometer *via* monochromatic Al Kα radiation. Peak positions were regulated using the C 1s peak at 284.8 eV *via* Casa XPSTM software. The intensity of the solar light was measured by a solar radiation meter.

2.5 Solar assisted photocatalysis

The photocatalytic performance of $Cu_{1-x}Fe_xS$ was investigated under direct solar light with an average intensity of 17 mW cm^{-2}. The Cr^{VI} reduction experiment, both in diffused and direct solar light, was conducted in a Pyrex glass of 100 mL capacity. The reduction reactions were examined by observing the changes in the UV-vis absorbance with the main absorption peak appearing at 352 nm. An aqueous solution of $K_2Cr_2O_7$ was taken as a standard source of Cr^{VI}. About 1 mL of formic acid (23 g L^{-1}) was added to 40 mL of an aqueous $K_2Cr_2O_7$ solution (100 mg L^{-1}) in a beaker followed by vigorous stirring at room temperature (25 °C) with the pH of the solution maintained at

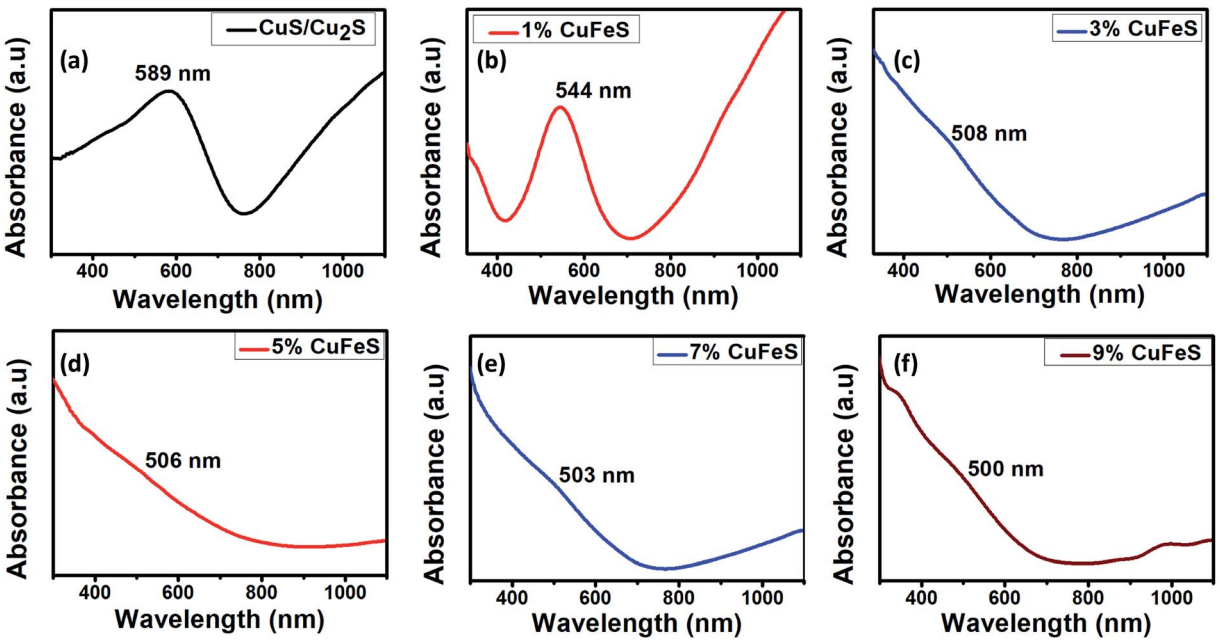

Fig. 2 UV-vis absorption images of (a) pure CuS/Cu_2S, (b) Fe (0.01)-CuS/Cu_2S, (c) Fe (0.03)-CuS/Cu_2S, (d) Fe (0.05)-CuS/Cu_2S, (e) Fe (0.07)-CuS/Cu_2S and (f) Fe (0.09)-CuS/Cu_2S.

2.5. At this point, the UV-visible spectrum of the solution mixture was recorded and was denoted as the 0 min data point. 0.01 g (10 mg/40 mL) of the synthesized $Cu_{1-x}Fe_xS$ ($x = 0$, 1, 3, 5, 7, 9%) nanocatalysts were added to the solution under sunlight with constant stirring. After every 2 min interval, about 3 mL of the solution was collected into an UV-vis cuvette and spectroscopically examined.

3. Results and discussion

3.1 XRD analysis

Fig. 1 shows the crystallographic structures of the pristine CuS/Cu_2S and Fe-doped CuS/Cu_2S nanostructures, synthesized at 180 °C. The diffraction patterns with 2θ values positioned at 46.2° and 55.2° correspond to the (*hkl*) planes of the (110) and (201) of the hexagonal *chalcocite* (Cu_2S) system {JCPDS no. 00-026-1116, space group $P6_3/mmc$ (194)} while the peaks at 27.3° and 32.4° matched well with the (*hkl*) plane of (100) and (006) of *covellite* (CuS) {JCPDS card no. 06-0464, space group $P6_3/mmc$ (194)}. No other phases were observed in the XRD spectra except for the hexagonal phase of CuS/Cu_2S. The formation of Cu_2S together with CuS is due to the reducing nature of ethylenediamine.[15] Notable changes in the (100) and (110) diffraction peaks were observed. A reduction in the intensity of the (110) peak accompanied by an increase in the intensity of the (100) upon increasing the concentration of dopant indicated the key morphological changes in the material, most probably due to the lattice contractions. The broadening of the XRD peaks of the Fe-doped CuS/Cu_2S NPs compared to those of pristine CuS shows the decrease in size of the nanoparticles with Fe dosage. The 2θ positions also shifted with an increase in Fe doping, which can be credited to the smaller ionic radii of Fe^{2+} (0.064 nm) compared to that of Cu^{2+} (0.065 nm). Furthermore, the average crystallite size (D) could be calculated using the FWHM (Full Width Half Maximum) of the diffraction peaks by using the Debye–Scherrer formula (eqn (1)),

$$D = 0.9\lambda/B\cos\theta \quad (1)$$

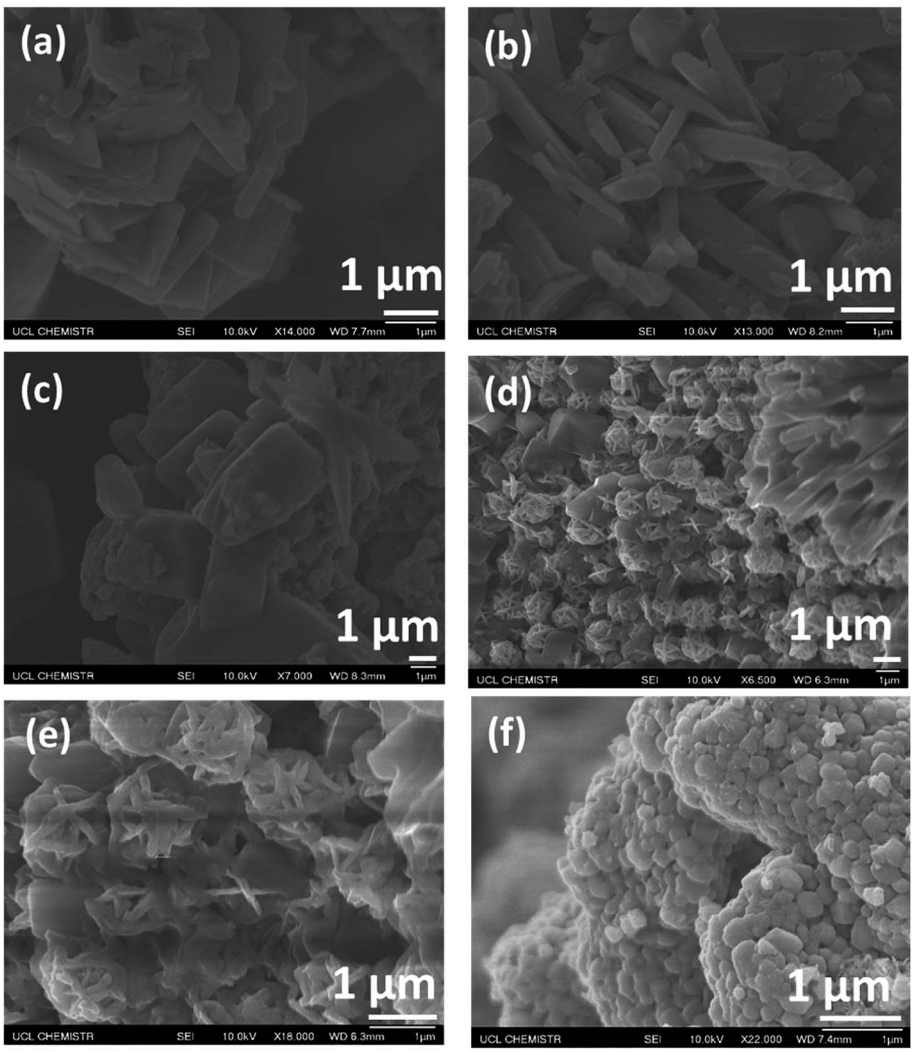

Fig. 3 SEM images of (a) pure CuS/Cu_2S, (b) Fe (0.01)-CuS/Cu_2S, (c) Fe (0.03)-CuS/Cu_2S, (d) Fe (0.05)-CuS/Cu_2S, (e) Fe (0.07)-CuS/Cu_2S and (f) Fe (0.09)-CuS/Cu_2S.

where θ and λ are the diffraction angle and the wavelength of Cu Kα radiation ($\lambda = 1.54178$ Å) used as a source, respectively. The average crystallite sizes calculated for each dopant were found in the range of 10.51 to 21.96 nm.

3.2 Optical analysis

UV-visible spectrophotometry is one of the most useful techniques to investigate the optical properties of nanoparticles. The absorption spectra of the synthesized nanoparticles lie in the visible region (Fig. 2), that makes them promising photocatalysts. For pristine CuS/Cu_2S, the absorption edge was observed at 589 nm, *i.e.*, there is a blue shift compared to bulk CuS (1032 nm).[16] Likewise, with the addition of the dopant, there is a noticeable blue shift observed, indicating an enhancement in the band gap. This enhancement is due to sp-d exchange interactions among localized d-electrons of the dopant (Fe^{2+}) and the CuS band electrons.[17] Increases in absorption intensity after 600 nm up to the near IR region were observed owing to a surface plasmonic resonance (SPR), a distinctive characteristic of the *covellite* phase of CuS nanoparticles.[18,19] The energy band gap "E_g" was calculated using Planck's equation, $E_g = hc/\lambda$ where h is the Planck's constant, c is the speed of light and λ is the wavelength at which the maximum absorbance occurs.[20] The calculated band gaps of the doped $Cu_{1-x}Fe_xS$ ($x = 0$, 1, 3, 5, 7 and 9%) nanoparticles were 2.1, 2.27, 2.44, 2.45, 2.46 and 2.48 eV, respectively.

3.3 Structural characterization

Scanning electron microscopy is an excellent way of examining the morphologies of nanoparticles by monitoring the cross sections of samples. Fig. 3a–f illustrates the SEM images of the 0–9% Fe-doped CuS/Cu_2S NPs. On the basis of these results, it can be assumed that the Fe has considerable control over the morphologies of the particles, which may be due to the significant reactions of iron under solvothermal conditions. The morphology of pristine CuS/Cu_2S NPs is plate-like with a particle size around 1 μm. Once Fe is introduced, the morphology transforms completely as compared to that of the pristine copper sulfide nanoparticles. The increase in doping has clearly changed the morphology from plates to rods and then finally to flowers and spheres with a decrease in size.

3.4 Energy dispersive X-ray spectroscopy (EDX) analysis

The compositions of the Fe-doped CuS/Cu_2S samples were studied using energy dispersive X-ray spectroscopy (EDX). Fig. S1 (ESI†) shows the EDX results for pure and the 1, 3, 5, 7, 9% Fe-doped CuS/Cu_2S nanoparticles. The stoichiometric ratios of Cu, S and Fe from these data are as expected, thus indicating the absence of any other elements in the nanoparticles. There was a contribution from C and O from the sample mounting tape. Eliminating the percentages of C and O enabled us to establish the purity of the Fe doped CuS/Cu_2S nanoparticles.

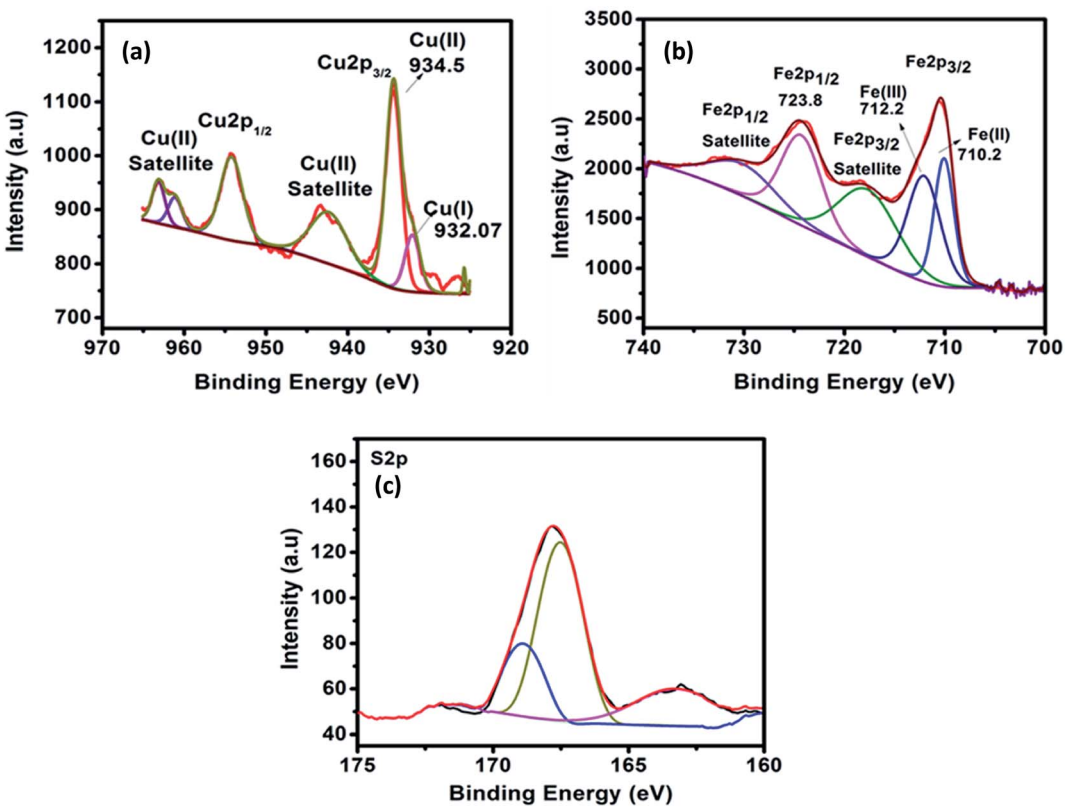

Fig. 4 XPS spectra and fitted results of (a) Cu2$p_{3/2}$, Cu2$p_{1/2}$, (b) Fe 2$p_{3/2}$, Fe 2$p_{1/2}$ and (c) S 2p.

3.5 X-ray photoelectron spectroscopy (XPS)

High resolution X-ray photoelectron spectroscopy was employed to determine the chemical composition and valance states on the surface of the Fe doped CuS/Cu_2S. Fig. 4a–c shows the core level spectra of Cu 2p, Fe 2p and S 2p. The core level spectra of Cu 2p (Fig. 4a) shows two major peaks at 934.5 eV and 954.5 eV due to the spin orbit splitting of Cu 2p into Cu $2p_{3/2}$ and Cu $2p_{1/2}$, respectively. In addition, the Cu $2p_{3/2}$ shows a small shoulder peak so it is further deconvoluted into two peaks located at 932.7 eV and 934.5 eV which correspond to the monovalent and divalent Cu species. The presence of satellite peaks (942.4 eV and 962.5 eV) confirms the existence of Cu^{2+} species. It is observed from the main and satellites peaks that the Cu^{2+} species are in a higher ratio than Cu^{+}, which thus further confirms that the formation of CuS is more pronounced than that of Cu_2S. Fig. 4b shows the Fe 2p core level spectra. The peaks for Fe 2p are well defined and broad due to the high concentration of doping (9%) and can further be deconvoluted. The peaks located at 710.8 eV and 723.8 eV are attributed to the Fe $2p_{3/2}$ and Fe $2p_{1/2}$, respectively. The satellite peaks located at higher binding energies (718.8 eV and 733.1 eV) indicate that the Fe ion is in a divalent state. The broad Fe $2p_{3/2}$ peak was deconvoluted into two peaks at 710.2 eV and 712.2 eV and could be assigned to divalent and trivalent Fe $2p_{3/2}$, respectively. The core level spectra of S 2p (Fig. 4c) is deconvoluted using a spin–orbit separation of 1.0 eV. The peaks at position 161.4 eV and 162.5 eV are merged into a single broad peak that appeared at 162.7 eV and can be assigned to the S 2p state of S^{2-} ions, which verifies the coordination of S with Cu in CuS.[21] Besides, a strong peak located at 168.3 eV can be assigned to the other species of S.

4. Photocatalytic reduction of Cr^{VI}

The photoreduction efficiencies of the undoped and Fe-doped (1, 3, 5, 7, 9%) CuS/Cu_2S nanoparticles were assessed by studying the reduction of Cr(VI) (10^{-4} M $K_2Cr_2O_7$) using a UV vis spectrophotometer under different experimental conditions. The reaction's progress was recorded by monitoring the behavior of the typical peak (352 nm) of Cr^{VI} over time. The effect of formic acid on the removal of Cr^{VI} was examined in the absence of the doped CuS/Cu_2S NPs and no significant reduction occurred even after 24 h at room temperature. Similarly, in the absence of formic acid, the Cr^{VI} reduction proceeded slowly, indicating clearly that Cr^{VI} reduction could not be achieved using the catalyst alone (Fig. 5).

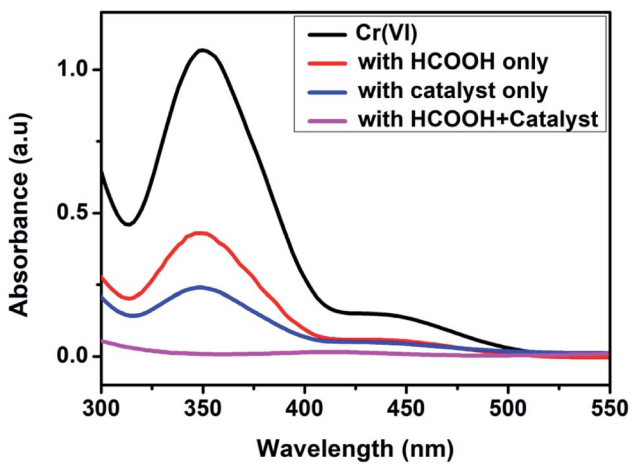

Fig. 5 Behavior of the Cr(VI) peak in the UV-vis spectra in the presence and absence of the catalyst and HCOOH.

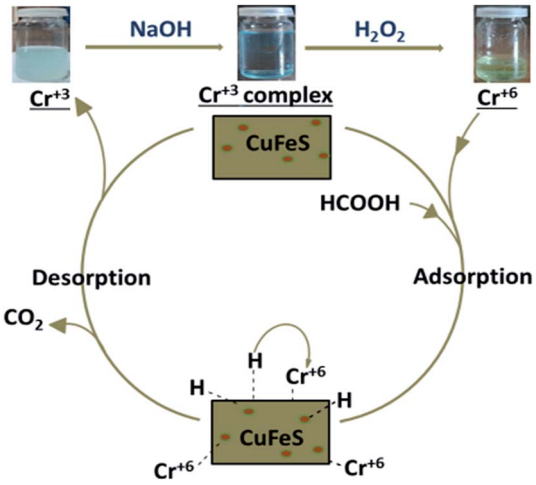

Fig. 6 The color change of the Cr(VI) solution.

With the addition of catalyst together with formic acid, the absorption band at 352 nm diminished gradually and eventually a change in color from yellow to colorless, substantiated the Cr^{VI} reduction to Cr^{III}.[22–23] After reduction, the presence of trivalent chromium was demonstrated by the addition of excess NaOH. The formation of hexahydroxochromate(III) ions resulted in the appearance of a blue-green solution,[23] which upon slight warming with the oxidant H_2O_2, resulted in a color change to yellow, confirming oxidation of the Cr(III) back to Cr(VI),[24] as shown in Fig. 6.

4.1 Photocatalytic activity in solar and diffused light

The photocatalytic performance of the synthesized nanoparticles in the Cr^{VI} to Cr^{III} reductions was studied under sunlight and diffused light. About 90% of the Cr^{VI} was removed by pristine CuS/Cu_2S under sunlight in 56 min, while only 62% was reduced under diffused light. It is worth noting that the Cr^{VI} conversion efficiency was considerably improved with an increase in the Fe doping in the copper sulfide NPs. All five doped $Cu_{1-x}Fe_xS$ nanostructures ($x = 1$, 3, 5, 7 and 9%) showed a 100% reduction according to the UV-vis spectra in both sunlight and diffused light. With an increase in the percentage of dopant (Fe^{2+}), a remarkable enhancement in the performance of the catalyst was observed. Among all the synthesized catalysts, the 9% doped sample showed the best performance. In sunlight, a complete reduction was observed in 6 min, while in diffused light the reduction took 9 min. Moreover, the

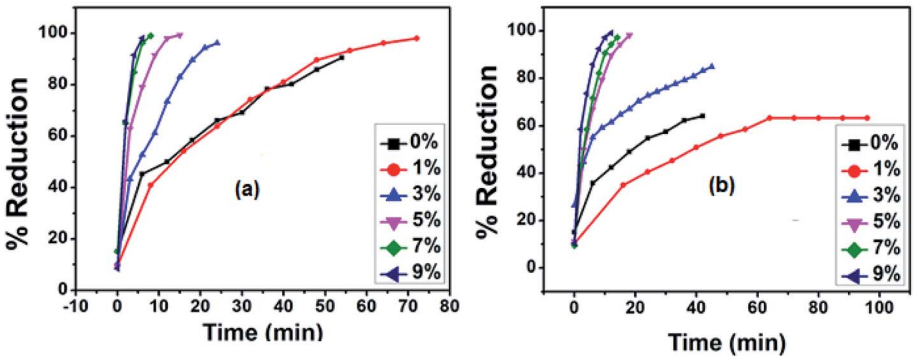

Fig. 7 Plots for the concentration change of Cr(VI) with time for CuS/Cu_2S and 1%, 3%, 5%, 7% and 9% Fe doped CuS/Cu_2S NPs (a) in sunlight (b) in diffused light.

photocatalytic performance of each of the five $Cu_{1-x}Fe_xS$ nanostructures in diffused light was lower than that under sunlight (Fig. 7).

4.2 Effect of pH

The pH plays a key part in the photocatalysis as it effects the surface charge of the catalyst, thus directly affecting the adsorption, photoreduction and interfacial electron transfer processes.[25] In our experiments, HCOOH functioned as a reductant and also performed an imperative role in regulating the pH of the reaction medium. The pH of the solutions was varied as 2.5, 3 and 4 by the addition of 1 M NaOH solution. A drastic decrease in the reduction rate was observed with an increase in pH, which agrees with the mechanism for Cr^{VI} reduction. The impact of pH on the photoreduction of Cr^{VI} was studied for 9% Fe-doped CuS nanoparticles with the fastest photoreduction occurring at pH 2.5. At low pH, there will be an excess of H^+ ions that will boost the reduction rate.[26]

$$Cr_2O_7^{2-} + 8H^+ + 3HCOOH \rightarrow 2Cr^{3+} + 7H_2O + 3CO_2 \quad (2)$$

At high pH, however, excess OH^- ions become adsorbed on the catalyst surface and inhibit the dichromate oxyanions reaching the surface of the catalyst, resulting in a reduced rate of adsorption of the Cr^{VI} species and consequently a reduced Cr^{VI} reduction. Moreover, Cr^{VI} can be spontaneously reduced in acidic media due to its high redox potential, 1.33 eV. The mechanism for Cr^{VI} reduction involves the adsorption of oxyanions of Cr(VI), *e.g.*, CrO_4^{2-}, $HCrO_4^{1-}$ and $Cr_2O_7^{2-}$, by electrostatic attraction, since at a pH less than the point of zero charge (PZC), the CuS catalyst bears a positive charge. For CuS, a pH of 5.2 value is reported to be the PZC, which is why the surface of CuS bears a negative charge above pH 5.2 owing to the adsorbed OH^- ions. At pH below 5.2 (under acidic conditions), the CuS catalyst has a positive charge.[27]

Thus, the efficacy of the catalyst for Cr^{VI} photoreduction is less at elevated pH values. Additionally, the poisoning of the photocatalyst may occur at a basic pH owing to the deposition of Cr^{III} as $Cr(OH)_3$ on the photocatalyst surface (Fig. 8).

4.3 Effect of catalyst's amount

The catalyst amount is one of the key factors in enhancing the reduction conditions. In our experiments, the impact of the catalyst on the reduction of Cr^{VI} was examined using a catalyst dosage varying from 2.5 to 10 mg to evade an ineffective surplus amount of the catalyst (Fig. 9).

The results clearly indicated the gradual increase in the photocatalytic reduction of Cr^{VI} with the amount of catalyst. This situation may be attributed to the number of active sites on the surface of the photocatalyst and the penetration of the

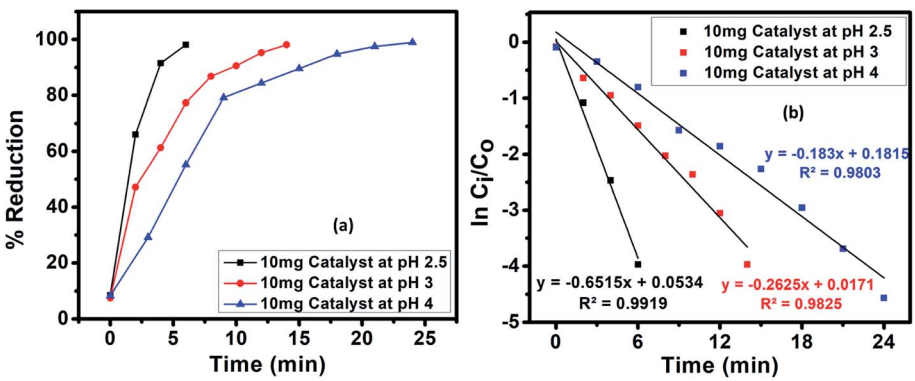

Fig. 8 (a) Effect of pH on the solar-assisted catalytic reduction of Cr(VI) using an initial concentration of 100 mg L^{-1} of Cr(VI) and (b) the pseudo-first-order graph of $\ln(C_i/C_0)$ *versus* time for the Cr(VI) photocatalytic reduction.

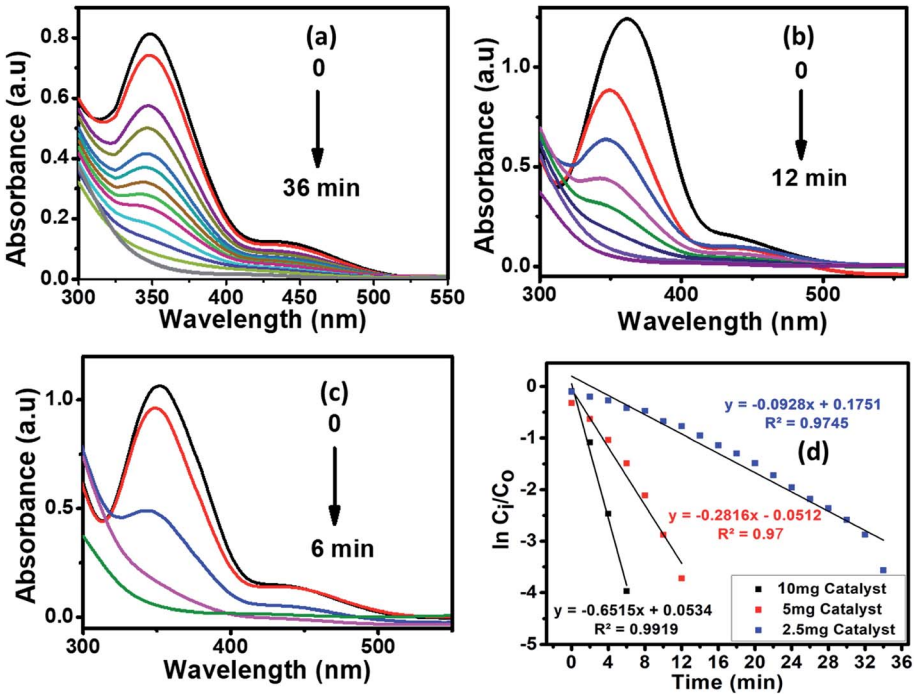

Fig. 9 The photocatalytic reduction of aqueous Cr(VI) using HCOOH as the reducing agent, in the presence of various amounts (a) 2.5, (b) 5, (c) 10 mg of $Cu_{1-x}Fe_xS$ as the catalyst (where $x = 9\%$) and (d) the pseudo-first-order graph of $\ln(C_i/C_0)$ *versus* time for the Cr(VI) photocatalytic reduction.

visible light through the solution. The kinetics of the Cr^{VI} reduction by $Cu_{1-x}Fe_xS$ are illustrated in the Fig. 9 inset. A pseudo-first-order kinetic equation (eqn (3)) was applied to the hexavalent chromium reduction in the presence of an excess of formic acid.

$$\ln C_i/C_0 = -kt \quad (3)$$

where k represents the apparent rate constant (min^{-1}), C_i is the dichromate ion concentration at reaction time "t" and C_0 is the initial concentration of the dichromate ion.

4.4 Effect of temperature

The influence of temperature on the Cr^{VI} reduction was studied by reacting 40 mL of 10^{-4} M Cr^{VI} with 10 mg $Cu_{1-x}Fe_xS$ ($x = 9\%$) nanoparticles and 1 mL of 4.99×10^2 mM HCOOH at 35, 40 and 45 °C (Fig. 10). With increasing temperature, the conversion of Cr^{VI} to Cr^{III} was significantly improved (Fig. S2†) with a 100% conversion attained at 45 °C. This clearly indicated that higher temperatures can enhance the activity of the catalyst[28] due to an increase in the accessible active surface area of the photocatalyst.[29] This state of affairs arises because of the increased decomposition of formic acid to nascent hydrogen [H] at elevated temperatures, which also leads to an increase in the surface acidity of the catalyst, further accelerating the reduction reaction.[30]

4.5 Stability of the catalyst

The catalyst's stability was tested for five cycles and the results revealed that, in all cycles, Cr^{VI} was almost completely reduced,

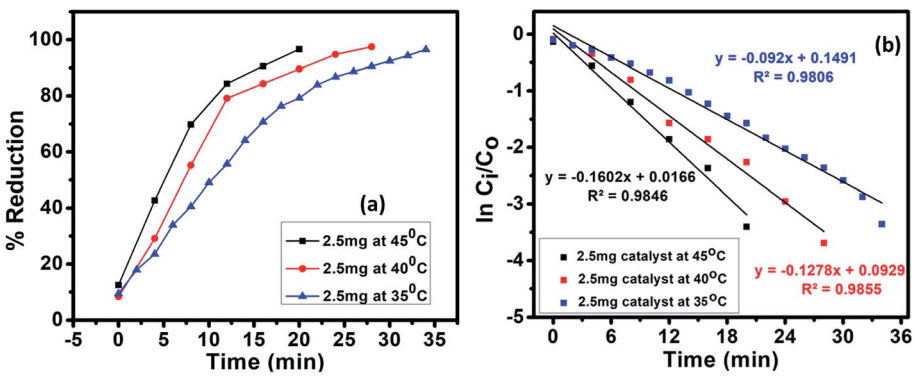

Fig. 10 (a) Effect of temperature on the solar assisted catalytic reduction of Cr(VI) using an initial concentration of 100 mg L^{-1} of Cr(VI) and (b) the pseudo-first-order graph of $\ln(C_i/C_0)$ *versus* time for Cr(VI) photocatalytic reduction.

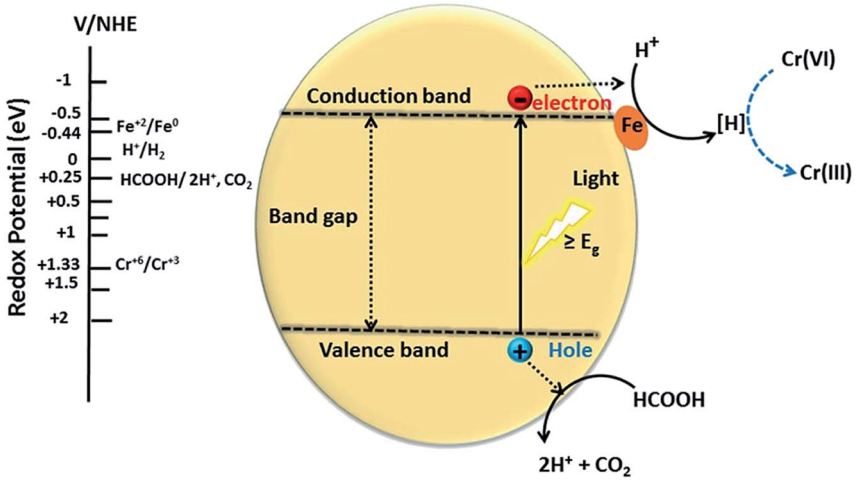

Fig. 11 Proposed mechanism for the photocatalytic reduction of Cr(VI) over $Cu_{1-x}Fe_xS$.

but it took a bit longer time wise (Fig. S3†). This small loss in stability is attributed to a slight loss of the catalyst during the cycling process. The XRD results for $Cu_{1-x}Fe_xS$ ($x = 9\%$), shown in Fig. S4 (ESI†), confirmed the stability and reusability of the catalyst. Therefore, the $Cu_{1-x}Fe_xS$ ($x = 9\%$) catalyst does exhibit considerable potential for the purification of contaminated water containing Cr^{VI} ions.

4.6 Proposed mechanism for the reduction of Cr^{VI} on $Cu_{1-x}Fe_xS$

A proposed mechanism for the conversion of Cr^{VI} to Cr^{III} using $Cu_{1-x}Fe_xS$ nanostructures is given in Fig. 11. This mechanism assumes that the CuS/Cu_2S nanoparticles are the active centers for reduction. Photoexcitation of electrons to the CB leaves behind positive holes (h^+) that facilitate the decomposition of the formic acid adsorbed on the surface of the catalyst to CO_2 and hydrogen ion (H^+). The photoexcited electrons are trapped by the dopant (Fe^{2+}) to reduce hydrogen ions (H^+) to nascent hydrogen [H] that subsequently reduces Cr^{VI} to Cr^{III}.

The dopant (Fe^{2+}) on the surface of the CuS acts as a co-catalyst that scavenges photoexcited electrons from the CB, thus facilitating an electron-transfer process in reduction and preventing the electron–hole recombination. The photo-excited electrons from the CB progress to the catalyst surface and transform the hydrogen ion to nascent hydrogen [H]. This hydrogen radical is highly reactive and efficiently reduces the Cr^{VI} of $Cr_2O_7^{2-}$ to Cr^{III} with water as a by-product:

$$3HCOOH_{(aq)} \rightarrow 2CO_2 + 6e^- + 6H^+ \quad (4)$$

$$Cr_2O_7^{2-} + 14H^+ + 6e^- \rightarrow 2Cr^{3+} + 7H_2O \quad (5)$$

Formic acid has a reduction potential (+0.25 eV) that is less positive or more negative than the CuS VB reduction potential (+2.05 eV). Consequently, CuS can oxidize HCOOH to CO_2 and H^+. On the other hand, the reduction potential of Fe^{2+}/Fe^0 (−0.44 eV) is more positive than the CuS CB reduction potential (−0.5 eV), so the transfer of electrons from the CB of CuS to the Fe^{2+} (dopant) is feasible due to the band off-set. The Fe^0, therefore, provides a stable platform to reduce the protons to nascent hydrogen [H], which in turn acts as a reductant for hexavalent chromium.[11,26,31]

4.7 Apparent rate constant dependence on temperature

To observe the detailed kinetics of the Cr^{VI} photocatalytic reduction, the temperature dependence of the Langmuir–Hinshelwood mechanism was examined for $Cu_{1-x}Fe_xS$ ($x = 9\%$) nanoparticles. The hexavalent chromium reduction was performed at three different temperatures (35, 40 and 45 °C). The E_a (43 kJ mol^{-1}) was calculated from the Arrhenius equation *i.e.*, $\ln k = \ln A - E_a/RT$, by plotting $\ln k$ *vs.* $1/T$ (Fig. S5†). The kinetic

Table 1 Comparison of the present work with the literature

S. no.	Nanomaterial	Catalyst loading	Cr(VI) concentration	Time (min)	% reduction	Reference
1	9% Fe doped CuS/Cu_2S	2.5 mg/40 mL, 5 mg/40 mL, 10 mg/40 mL	100 ppm	36, 12, 6	100%	Our work
2	CM-*n*-TiO_2	0.5 g L^{-1}, 1 g L^{-1}, 1.5 g L^{-1}, 2.0 g L^{-1}, 2.5 g L^{-1}	3 ppm	240, 120, 105, 30, 10	100%	32
3	C_{ZnO}-dots	3 mg mL^{-1}	100 ppm	300	100%	33
4	TiO_2	1 g L^{-1}	100 ppm, 500 ppm	120	89%, 84%	34
5	FeOOH	0.5 g L^{-1}	20 ppm	120	100%	35

parameters, activation entropy ($\Delta S^{\#}$) and enthalpy ($\Delta H^{\#}$), were calculated using the Eyring equation *i.e.*, $\ln k/T = \ln(k_b/h) + \Delta S^{\#}/R - \Delta H^{\#}/R(1/T)$. The plot of $\ln k_{app}/T$ *vs.* $1/T$ (Fig. S6†) have given a straight line with slope $-\Delta H^{\#}/R$ and intercept $(\ln(k_b/h) + \Delta S^{\#}/R)$ from which $-\Delta H^{\#}$ (156 kJ mol^{-1}) and $\Delta S^{\#}$ (-197.51 J mol^{-1} K^{-1}) were calculated. The positive $\Delta H^{\#}$ value reflects the endothermic nature of the reduction process.

The Fe doped CuS/Cu_2S nanoplates are superior to previously reported[32–35] nanoparticles (Table 1) for Cr^{VI} reduction: a 100% Cr reduction with a very small amount of catalyst in much less time. Iron doping improved the morphologies of NPs to provide a high contact area to trigger the reduction process with more surface atoms and unsatisfied valences. The iron dopant further enhanced the reduction process by acting as electron scavenger that prevented electron hole recombination.

5. Conclusions

The results presented in this paper suggest that Fe as a dopant not only induced the morphological change in the CuS/Cu_2S lattice, but also created a morphology-dependent redox shuttle mechanism. This morphology-dependent photoreduction of Cr^{VI} by $Cu_{1-x}Fe_xS$ NPs under solar light irradiation is, indeed, a novel technique for harvesting solar energy and for the reduction of toxic Cr^{VI} ions in wastewater. Furthermore, $Cu_{1-x}Fe_xS$ is a more efficient photocatalyst than the pristine CuS/Cu_2S and other reported photocatalysts. This is because of the suitable reduction potential of Fe that facilitates electron transfer between CuS and H^+ (generated from the oxidation of HCOOH by a hole). For $Cu_{1-x}Fe_xS$, a high activity was found at a high dopant concentration (9%), low pH (2.5) and elevated temperature.

Conflicts of interest

There is no conflict of interest.

Acknowledgements

We are thankful to the Higher Education Commission of Pakistan for their financial support.

References

1 J. C. Crittenden, Y. Zhang, D. W. Hand, D. L. Perram and E. G. Marchand, *Water Environ. Res.*, 1996, **68**, 270–278.
2 L. Khalil, W. Mourad and M. Rophael, *Appl. Catal., B*, 1998, **17**, 267–273.
3 S. N. Frank and A. J. Bard, *J. Phys. Chem.*, 1977, **81**, 1484–1488.
4 K. I. Okamoto, Y. Yamamoto, H. Tanaka, M. Tanaka and A. Itaya, *Bull. Chem. Soc. Jpn.*, 1985, **58**, 2015–2022.
5 J. Domenech and J. Costa, *Photochem. Photobiol.*, 1986, **44**, 675–677.
6 J. Doménech and A. Prieto, *Electrochim. Acta*, 1986, **31**, 1317–1320.
7 Y. Deng, L. Tang, G. Zeng, Z. Zhu, M. Yan, Y. Zhou, J. Wang, Y. Liu and J. Wang, *Appl. Catal., B*, 2017, **203**, 343–354.
8 L. Shi, T. Wang, H. Zhang, K. Chang, X. Meng, H. Liu and J. Ye, *Adv. Sci.*, 2015, **2**, 1500006.
9 H. Akcay, A. Oguz and C. Karapire, *Water Res.*, 2003, **37**, 813–822.
10 Y. Ku and I. L. Jung, *Water Res.*, 2001, **35**, 135–142.
11 N. Sreelekha, K. Subramanyam, D. A. Reddy, G. Murali, K. R. Varma and R. Vijayalakshmi, *Solid State Sci.*, 2016, **62**, 71–81.
12 Z. K. Heiba and M. B. Mohamed, *Appl. Phys. A: Mater. Sci. Process.*, 2018, **6**, 124.
13 A. Stroyuk, A. Kryukov, S. Y. Kuchmii and V. Pokhodenko, *Theor. Exp. Chem.*, 2005, **41**, 67–91.
14 N. u. Ain, Z. u. Rehman, A. Aamir, Y. Khan, M. u. Rehman and D. J. Laen, *Mater. Chem. Phys.*, 2020, **242**, 122408.
15 S. Gorai, D. Ganguli and S. Chaudhuri, *Cryst. Growth Des.*, 2005, **5**, 875–877.
16 Q. Lu, F. Gao and D. Zhao, *Nano Lett.*, 2002, **2**, 725–728.
17 B. Poornaprakash, D. A. Reddy, G. Murali, R. Vijayalakshmi and B. Reddy, *Phys. E*, 2015, **73**, 63–68.
18 Y. Zhao, H. Pan, Y. Lou, X. Qiu, J. Zhu and C. Burda, *J. Am. Chem. Soc.*, 2009, **131**, 4253–4261.
19 E. Dilena, D. Dorfs, C. George, K. Miszta, M. Povia, A. Genovese, A. Casu, M. Prato and L. Manna, *J. Mater. Chem.*, 2012, **22**, 13023–13031.
20 X. S. Hu, Y. Shen, L. H. Xu, L. M. Wang and Y. J. Xing, *J. Alloys Compd.*, 2016, **674**, 289–294.
21 F. Han, W. C. Li, D. Li and A. H. Lu, *ChemElectroChem*, 2014, **1**, 733–740.
22 H. Saikia, B. J. Borah, Y. Yamada and P. Bharali, *J. Colloid Interface Sci.*, 2017, **486**, 46–57.
23 Y. Guo, D. Wang, X. Liu, X. Wang, W. Liu and W. Qin, *New J. Chem.*, 2014, **38**, 5861–5867.
24 L. Liu, J. Xue, X. Shan, G. He, X. Wang and H. Chen, *Catal. Commun.*, 2016, **75**, 13–17.
25 M. C. Lu, G. D. Roam, J. N. Chen and C. Huang, *J. Photochem. Photobiol., A*, 1993, **76**, 103–110.
26 T. Xu, J. Xue, X. Zhang, G. He and H. Chen, *Appl. Surf. Sci.*, 2017, **402**, 294–300.
27 A. Nezamzadeh-Ejhieh and N. Moazzeni, *J. Ind. Eng. Chem.*, 2013, **19**, 1433–1442.
28 M. A. Omole, I. O. K'Owino and O. A. Sadik, *Appl. Catal., B*, 2007, **76**, 158–167.
29 J. Wen, X. Li, W. Liu, Y. Fang, J. Xie and Y. Xu, *Chin. J. Catal.*, 2015, **36**, 2049–2070.
30 S. Li, L. Tang, G. Zeng, J. Wang, Y. Deng, J. Wang, Z. Xie and Y. Zhou, *Environ. Sci. Pollut. Res.*, 2016, **23**, 22027–22036.
31 K. Bhowmik, A. Mukherjee, M. K. Mishra and G. De, *Langmuir*, 2014, **30**, 3209–3216.
32 Y. A. Shaban, *World J. Nano Sci. Eng.*, 2013, **3**, 154.
33 P. Khare, A. Bhati, S. R. Anand, Gunture and S. K. Sonkar, *ACS Omega*, 2018, **3**, 5187–5194.
34 M. A. Ahmed, A. T. Elsir, F. Mohammed, H. Elbushra, S. Tawer and N. Eassa, *MRS Adv.*, 2018, **3**, 2667–2674.
35 M. R. Samarghandi, J. K. Yang, O. Giahi and M. Shirzad-Siboni, *Environ. Technol.*, 2015, **36**, 1132–1140.

